

Probing Feedback via IGM tomography and Ly α forest with Subaru PFS, TMT/ELT, & JWST

KENTARO NAGAMINE,^{1,2,3} IKKOH SHIMIZU,⁴ KATSUMI FUJITA,¹ NAO SUZUKI,² KHEE-GAN LEE,² RIEKO MOMOSE,⁵ SHIRO MUKAE,^{6,5} YONGMING LIANG,^{5,7} NOBUNARI KASHIKAWA,⁵ MASAMI OUCHI,^{7,5,6} AND JOHN D. SILVERMAN²

¹*Theoretical Astrophysics, Department of Earth and Space Science, Graduate School of Science, Osaka University,
1-1 Machikaneyama, Toyonaka, Osaka 560-0043, Japan*

²*Kavli-IPMU (WPI), University of Tokyo, 5-1-5 Kashiwanoha, Kashiwa, Chiba, 277-8583, Japan*

³*Department of Physics & Astronomy, University of Nevada, Las Vegas, 4505 S. Maryland Pkwy, Las Vegas, NV 89154-4002, USA*

⁴*Shikoku Gakuin University, 3-2-1 Bunkyocho, Zentsuji, Kagawa, 765-8505, Japan*

⁵*Department of Astronomy, University of Tokyo, 7-3-1 Hongo, Bunkyo, Tokyo, 113-8654, Japan*

⁶*ICRR, University of Tokyo, 5-1-5 Kashiwanoha, Kashiwa, Chiba, 277-8582, Japan*

⁷*National Astronomical Observatory of Japan, Mitaka, Tokyo, Japan*

ABSTRACT

In preparation for the IGM tomography study by Subaru Prime Focus Spectrograph (PFS) survey and other large future telescopes such as TMT/ELT/GMT, we present the results of our pilot study on Lyman- α forest and IGM tomography statistics using the GADGET3-OSAKA cosmological smoothed particle hydrodynamical simulation. Our simulation includes models for star formation and supernova feedback, which enables more realistic cross-correlation studies between galaxies, neutral hydrogen (HI) and metals in circumgalactic and intergalactic medium. We create light-cone data set at $z = 2 - 3$ from our simulations and generate mock Ly α forest data. As a first step, in this paper, we focus on the distribution of HI and galaxies, and present statistical results on 1-D flux PDF, 1-D power spectrum, flux contrast vs. impact parameter, HI-galaxy cross-correlations. Our results show overall agreement with current observational data, with some interesting discrepancies on small scales which are due to either feedback effects or varying observational conditions. Our simulation shows stronger HI absorption with decreasing transverse distance from galaxies. Comparison with observations shows that the current observed data points include important contributions from lower mass galaxies of $M_{\star} \sim 10^8 - 10^{10} M_{\odot}$ rather than just from massive galaxies of $M_{\star} \geq 10^{10} M_{\odot}$, which dilutes the stronger signal of flux contrast around massive galaxies. On large scales, the average absorption decrement smoothly connects to the IGM level, supporting the concordance Λ cold dark matter model. We also find an increase in the HI absorption towards the center of proto-cluster.

Keywords: cosmology — intergalactic medium — neutral hydrogen — galaxy formation — numerical simulation

1. INTRODUCTION

Understanding the distribution of baryons and galaxies is one of the most important topics in modern cosmological studies. In particular, hydrogen is the most abundant element in our Universe, and the distribution of neutral hydrogen (HI) contains useful information on the radiative history of our Universe, e.g., the evolution of ultra-violet background (UVB) radiation field, cosmic star formation history, and the interaction

between galaxies, circum-galactic medium (CGM) and inter-galactic medium (IGM).

The HI gas at cosmological distances can be observed as Lyman- α (hereafter Ly α) forest in quasar absorption lines, and abundant data from high-resolution spectroscopy has been collected over the past few decades (e.g., Cowie et al. 1995). In conjunction with those observational efforts, cosmological hydrodynamic simulations have played crucial roles in deepening our understanding of the nature of Ly α forest clouds (Cen et al. 1994; Hernquist et al. 1996; Miralda-Escudé et al. 1996), and it is generally accepted that the Ly α forest originates from the diffuse HI gas in filamentary structures

as well as the gaseous clouds mildly bound by gravity (Ly-limit systems). The Ly α forest has proven to be one of the most powerful probes of cosmology, and it has been used to constrain the cosmological parameters (Weinberg et al. 1998; McDonald et al. 2006), the matter power spectrum (Croft et al. 1998; Iršič et al. 2017), the mass of warm dark matter particles (e.g. Viel et al. 2005, 2013a), the mass of neutrinos (Palanque-DeLabrouille et al. 2015), and the impact of supernova feedback on IGM (e.g. Theuns et al. 2002; Cen et al. 2005).

Over the past several years, by utilizing a large quasar catalogue from the Sloan Digital Sky Survey (SDSS-BOSS; Dawson et al. 2013, $\sim 160,000$ sight lines), significant HI overdensities (i.e. proto-cluster candidates) have been identified at $z = 2 - 3$ (Cai et al. 2016, 2017; Mukae et al. 2020; Ravoux et al. 2020), which are expected to be a more uniform, unbiased sample of proto-clusters, covering a large cosmological volume of $\sim \text{Gpc}^3$. (However, note the cautionary remarks by Miller et al. 2019 as well. See also Section 3.6 for related discussions.) These proto-clusters will serve as unique test beds for the hierarchical structure formation scenario (Overzier 2016; Chiang et al. 2017). For example, the most massive galaxies are found in proto-clusters, and they are expected to be the first ones to make transition from the star-forming blue sequence to the red-sequence. The connections between radio galaxies, Ly α blobs and proto-clusters are also of significant interest.

One can also perform the ‘IGM tomography’ using more ubiquitous bright star-forming galaxies (e.g., Ly-break galaxies [LBGs] at $z \sim 3$) as background sources, and measure the 3D distribution of HI gas in the foreground at $z = 2 - 3$. Indeed, Lee et al. (2014) have demonstrated that this can be done using the Keck telescope, i.e., the CLAMATO survey (Lee et al. 2018). A galaxy proto-cluster has been identified at $z = 2.44$ by the Ly α tomographic technique (Lee et al. 2016). The scientific goals of IGM tomography are: (i) to characterize the cosmic web at $z > 2$, (ii) to study the association between galaxies/AGN and HI gas, and (iii) to identify proto-clusters and voids in an unbiased fashion.

There are many large spectroscopic surveys being planned in the next decade to probe intermediate redshift range of $z > 1$. The Sloan Digital Sky Survey (SDSS) and 2-degree Field (2dF) surveys gave us excellent views of our local Universe, and the ‘SDSS at $z \sim 1$ ’ will soon become available by the combination of Subaru Hyper-Supreme Cam (HSC) and Prime Focus Spectrograph (PFS) projects (Takada et al. 2014). The Subaru PFS survey is a large spectroscopic survey on the Subaru telescope employing ~ 2400 fibers posi-

tioned across a 1.3 deg field, which is scheduled to start from ~ 2022 . It follows up on the ongoing HSC imaging survey, and the combination of the two large projects will present unique opportunities to study galaxy evolution and HI distribution in our Universe at the same time. The high- z program of the PFS project plans to cover the sky area of 15 deg^2 of the HSC deep fields, and is likely to include topics such as the IGM tomography at $z = 2 - 3$, galaxy evolution at $z = 2 - 6$, reionization studies using Ly α emitters (LAEs) at $z = 6 - 7$.

While there are other similar projects to the Subaru PFS utilizing multiplexed fiber spectrograph, such as the WEAVE (Dalton et al. 2012) and the MOONS (Cirasuolo et al. 2014), PFS has a unique combination of both telescope diameter and spectral coverage into the blue. This allows it to observe large numbers of galaxies at $z \sim 2 - 3$ and at the same time measure the Ly α forest absorption with large numbers of background sources.

In this paper, we focus on the science cases related to the PFS IGM tomography program, and prepare to make some forecasts using cosmological hydrodynamic simulations that include full physics of star formation and supernova (SN) feedback. Some details of other major projects such as JWST and ELT/TMT are summarized in Appendix.

For the IGM tomography, the spatial resolution of current observational study is still coarse, and numerical simulations can provide useful comparison data set, by making mock light-cone output and mimicing the actual observations to examine the expected observational results. For example, Lukić et al. (2015) used the NYX hydrodynamic simulation to examine the Ly α forest statistics, but without the treatment of star formation and feedback (i.e., an optically-thin calculation). They found that the hydrodynamic resolution of $20 h^{-1} \text{ kpc}$ is required to achieve 1 per cent convergence of Ly α forest flux statistics up to $k = 10 h \text{ Mpc}^{-1}$, and box sizes of $L > 40 h^{-1} \text{ cMpc}$ is needed to suppress the errors to sub-percent level for the 1D flux power spectrum. Typically, convergence of 5 – 10 per cent had been reported by several authors using box sizes of $20 - 40 h^{-1} \text{ cMpc}$ with resolutions of $50 - 200 h^{-1} \text{ ckpc}$ at $z \sim 2$ (e.g. Meiksin & White 2004; McDonald et al. 2005; Viel et al. 2006; Bolton & Becker 2009; Tytler et al. 2009).

Furthermore, Sorini et al. (2018) used the Illustris and NYX simulations to examine average Ly α absorption profile around galaxies, and showed that the results agree well with the observations by BOSS (Font-Ribera et al. 2013) and quasar pairs (Prochaska et al. 2013; Rubin et al. 2015) at transverse distances of $0.02 \lesssim b \lesssim 20 \text{ Mpc}$. They argued that the nice asymptotic agreement of the absorption profile on large scales is a re-

flection of the fact that the Λ CDM model successfully describes the distribution of ambient IGM around the dark matter halos. Based on the comparison between the simulations and observations, they also suggested that the ‘sphere of influence’ of galaxies could extend out to ~ 7 times the halo virial radius, i.e. to ~ 2 Mpc. Sorini et al. (2018) also showed that the both Illustris and NYX simulations underpredict the Ly α absorption profile around quasars and LBGs at small separations of $b < R_{\text{vir}}$. Sorini et al. (2020) further examined the SIMBA hydrodynamic simulation and showed that it overpredicts the absorption (i.e. flux contrast) on small scales of $b < 100$ kpc significantly. We show in this paper that our GADGET3-OSAKA simulation does not have these problems on small scales, and we highlight the variation caused by the differences in feedback models and galaxy samples.

An important difference of the present work over the earlier ones is that we use the cosmological hydrodynamic simulation with star formation and SN feedback (but no AGN feedback yet). The SHERWOOD simulation series (Bolton et al. 2017) operates at slightly higher resolution than our simulation, but they did not treat the star formation process in detail, and instead resorted to a simplified model of converting the highest density gas into star particles to save computing time. We also note that Sorini et al. (2020) found that the impact of AGN feedback is not so strong, and that the stellar feedback is the primary driver for determining the average physical properties of CGM at $z = 2 - 3$. Therefore the absence of AGN feedback treatment in the present paper is not so critical, as we are not discussing the proximity effect around quasars in particular (but see the discussion in Section 3.6).

As a pathfinder to the IGM tomography studies by the Subaru PFS and upcoming large telescopes such as TMT/ELT, we examine various statistics related to the Ly α forest, such as the 1D flux PDF, 1D power spectrum, Ly α decrement as a function of transverse distance from galaxies, and cross-correlation between galaxies and H I gas. This is only our first step towards more rigorous comparisons between simulations and observations of CGM & IGM. In this paper, we focus on the relative distribution of galaxies and H I, and do not touch on the metal absorption lines, which we will discuss in our later publications. The goal of this paper is not to argue for a best-fit simulation parameters or subgrid models, but rather to highlight the differences with the currently available observational data and look for the right directions for our future research. The astrophysics in this subject is quite rich, as we need to have a good understanding of cosmology, galaxy forma-

tion, star formation, feedback and chemical enrichment of the IGM, and link them all together to have a full picture.

The results presented in this paper serve as basis for our future work of comparing the simulations and observations, for example, as presented by Momose et al. (2020a,b) and Liang et al. (2020, submitted). We will refer to their results in more detail in later sections.

This paper is organized as follows. We describe the details of our cosmological hydrodynamic simulations in Section 2.1, and the method of generating the Ly α forest data is presented in Section 2.2. In Section 3, we lay out the results of Ly α flux PDF, 1D Ly α power spectrum, flux contrast vs. impact parameter from galaxies, cross-correlation between galaxies and H I, correlation between galaxy overdensity and Ly α absorption decrement, and finally the flux contrast in a proto-cluster. We then present our discussion and summary in Section 4.

2. SIMULATIONS AND METHODS

2.1. Cosmological Hydrodynamic Simulations

We use the GADGET3-OSAKA cosmological smoothed particle hydrodynamics (SPH) code (Aoyama et al. 2017; Shimizu et al. 2019), which is a modified version of GADGET-3 (originally described in Springel 2005, as GADGET-2). Our code includes models for star formation and SN feedback. We adopt the basic model of star formation in the AGORA project (Kim et al. 2014, 2016). The SN feedback recipe is described in detail by Shimizu et al. (2019), which we briefly summarize here. The feedback energy and metals are deposited within a hot bubble radius computed from a Sedov-Taylor-like solution which takes the cooling into account (Chevalier 1974; McKee & Ostriker 1977), similarly to the blast-wave model by Stinson et al. (2006). We also use the CELib chemical evolution library by Saitoh (2017) and appropriate time delays for Type Ia & II SNe, and AGB stars. The energy and metals are injected into the surrounding ISM with appropriate time delays for different sources based on CELib, following each star formation event. We compute the total feedback energy for each star-forming event, and deposit the energy in both thermal (70%) and kinetic (30%) form to the neighboring gas particle within the hot bubble radius, as in the fiducial model of Shimizu et al. (2019). Through the tests with isolated AGORA galaxies, we have found that this fiducial model has a moderate degree of chemical enrichment without overheating the IGM, unlike the original constant wind velocity model by Springel & Hernquist (2003). The merit of the Osaka feedback model is that the wind velocity and the hot bubble size is determined based on the local physical quantities (gas

Table 1. List of Numerical Simulations

Model	Notes
Osaka18-Fiducial	no self-shielding
Osaka18-Shield	with self-shielding
Osaka18-NoFB	no SN feedback
Osaka18-CW	Constant velocity galactic wind model ^a
Osaka18-FG09	UVB model of FG09 ^b

^aSpringel & Hernquist (2003, SH03)

^bFaucher-Giguère et al. (2009, FG09)

NOTE—Parameters of Osaka18 simulation series. All simulations use a box size of comoving $100 h^{-1}\text{Mpc}$ (cMpc), and 2×512^3 particles for gas and dark matter. Particle masses are $m_{\text{DM}} = 5.38 \times 10^8 h^{-1}\text{M}_{\odot}$ and $m_{\text{gas}} = 1.00 \times 10^8 h^{-1}\text{M}_{\odot}$. The first three runs adopt the Haardt & Madau (2012) UVB model. We also use a companion set of simulations with the same resolution and a box size of $50 h^{-1}\text{cMpc}$ for evaluating the box-size effect on our results.

density, pressure, available feedback energy) rather than bulk quantities such as galaxy stellar mass or halo mass, and this is more favorable for future higher resolution simulations.

The uniform UV radiation background model of Haardt & Madau (2012) is adopted. In one of the simulation runs, the self-shielding by optically-thick gas is treated following the prescription of Rahmati et al. (2013, which is based on the earlier similar works by Nagamine et al. 2010; Altay et al. 2011; Bird et al. 2013) to test its impact on the Ly α forest statistics. The cooling is solved by the Grackle chemistry and cooling library (Smith et al. 2017)¹ with the option of ‘`primordial_chemistry=3`’ which computes the detailed non-equilibrium chemistry network of 12-species. Metal cooling is also solved.

In this paper, we primarily use cosmological hydrodynamic simulations with a box size of $100 h^{-1}\text{Mpc}$ (comoving; hereafter cMpc) with total initial particle number of 2×512^3 . We also use another simulation with a box size of $50 h^{-1}\text{cMpc}$ and 2×256^3 particles to examine the box-size effect, but the results are very similar and we do not show the comparison here. Given the above parameters, the two simulations have exactly the same mass/spatial resolution, however, the $50 h^{-1}\text{cMpc}$ box is slightly too small to create the light-cone data set for the Ly α forest study at $z \approx 2 - 3$. We find

that we have sufficient resolution to resolve the Ly α forest in the wavelength space compared to the observations as we demonstrate later. The initial particle masses in the two simulations are $1.00 \times 10^8 h^{-1}\text{M}_{\odot}$ and $5.38 \times 10^8 h^{-1}\text{M}_{\odot}$ for gas and dark matter particles. The gas particle mass can change due to star formation and feedback. The gravitational softening length is set to $\epsilon_g = 7.8 h^{-1}\text{ckpc}$, but we allow the baryonic smoothing length to become as small as $0.1\epsilon_g$. This means that the minimum baryonic smoothing at $z = 2$ is about physical $260 h^{-1}\text{pc}$, which is sufficient to resolve the structures associated with Ly α forest. We adopt the following cosmological parameters from Planck Collaboration et al. (2016): $(\Omega_{\text{m}}, \Omega_{\text{dm}}, \Omega_{\text{b}}, \sigma_8, h) = (0.3089, 0.2603, 0.04860, 0.8150, 0.6776)$.

The list of simulations with different models are summarized in Table 1. Since the self-shielding of UVB might affect the Ly α forest via star formation and feedback (e.g., Theuns et al. 2002), we perform two runs with and without self-shielding: ‘Osaka18-Shield’ and ‘Osaka18-Fiducial’, respectively. The third run (Osaka18-NoFB) in Table 1 is without SN feedback to test the impact of Osaka feedback model on the Ly α forest statistics. The fourth run (Osaka18-CW) is with the constant velocity galactic wind model by Springel & Hernquist (2003). The fifth run (Osaka18-FG09) uses the UVB model of FG09 instead of Haardt & Madau (2012) to examine the impact of slight differences in the UVB model.

2.2. Light-cone & Line-of-Sight (LoS) data set

Using the output of our cosmological SPH simulations, we first produce the light-cone data set for a redshift path of $z \approx 2 - 3$ which is the primary redshift range of observed Ly α forest, as it conveniently falls into the optical wavelength range for ground-based spectroscopic observations. This is also the target redshift range for the IGM tomography by PFS (Takada et al. 2014). With JWST, we will be able to probe higher redshift range as well, but for the moment we focus on $z = 2 - 3$ in the present paper. We create the light-cone data by connecting 10 simulation boxes of different redshifts following Shimizu et al. (2016), and cover from $z \sim 1.8$ to 3.1 . When connecting the simulation boxes, we randomly shift and rotate each box so that the same structures do not repeat on a single line-of-sight (LoS). The resulting light-cone has transverse dimensions of $100 h^{-1}\text{cMpc} \times 100 h^{-1}\text{cMpc}$ and $1 h^{-1}\text{cGpc}$ sightline.

We then calculate the Ly α optical depth (τ) along the LoS. First, we calculate the physical quantities, $A_{\text{pixel}}(x)$, at each pixel x along LoS, such as H I den-

¹ <https://grackle.readthedocs.org/>

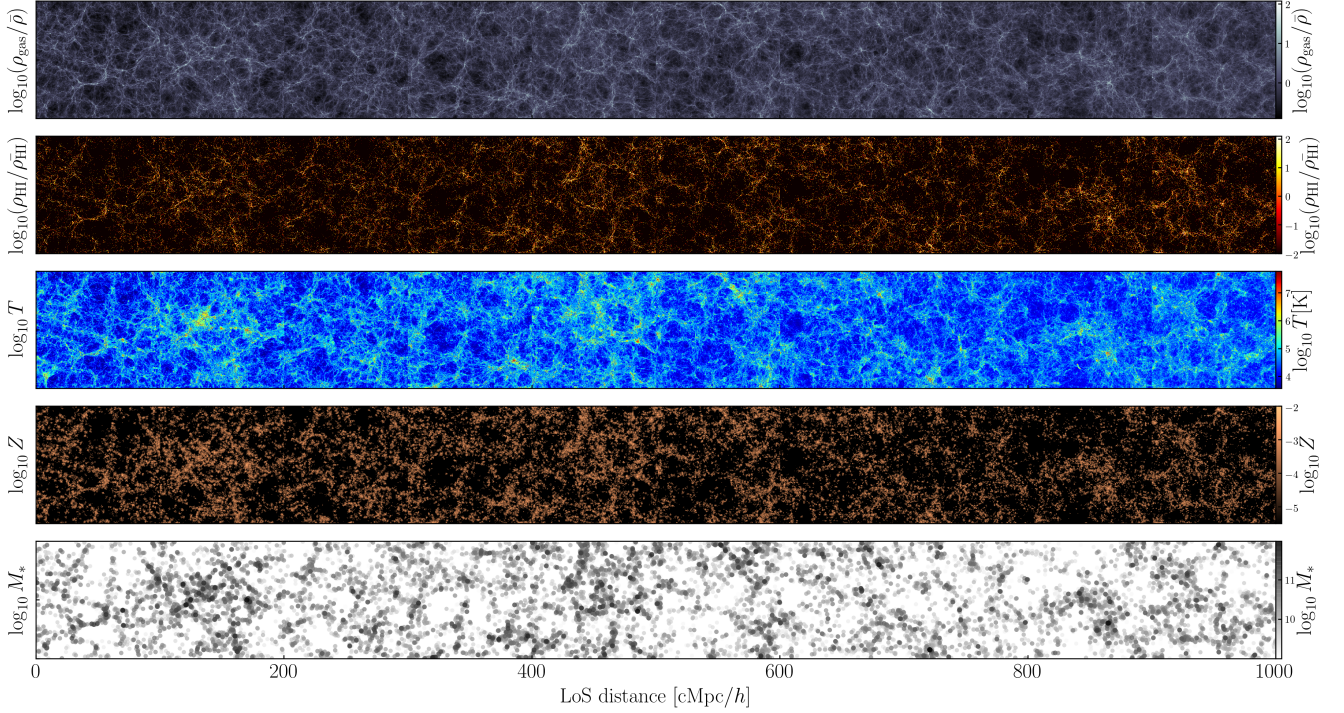


Figure 1. Light-cone output at $z \approx 2 - 3$, covering $100 h^{-1} \text{cMpc}$ (height) $\times 1 h^{-1} \text{cGpc}$ $\times 10 h^{-1} \text{cMpc}$ (depth). From top to bottom panels: projected gas overdensity, HI overdensity, temperature, metallicity, and galaxy distribution color-coded by the stellar mass, respectively. In the bottom panel, one can see the galaxy bias effect where more massive galaxies are more clustered in high-density regions.

sity, LoS velocity and temperature as follows:

$$A_{\text{pixel}}(x) = \sum_j \frac{m_j}{\rho_j} A_j W(r, h_j), \quad (1)$$

where A_j , m_j , ρ_j and h_j are the physical quantity of concern, gas particle mass, gas density, and smoothing length of j -th particle, respectively. W is the SPH kernel function, and r is the distance between LoS pixel and gas particles. The pixel length (dl) is set to a constant value of $100 h^{-1} \text{ckpc}$, which is higher resolution than any of the relevant Ly α observations. Then, we calculate the Ly α optical depth $\tau(x)$ using these physical values at each pixel as

$$\tau(x) = \frac{\pi e^2}{m_e c} \sum_j f_j \phi(x - x_j) n_{\text{HI}}(x_j) dl, \quad (2)$$

where e , m_e , c , f_j , n_{HI} , and x_j are the electron charge, electron mass, speed of light, absorption oscillator strength, HI number density, and j -th pixel location, respectively. ϕ is the Voigt profile, and we use the fitting formula of [Tasitsiomi \(2006\)](#) without direct integration. We draw 1024 ($= 32^2$) LoS with regularly spaced intervals, resulting in mean transverse separation of $3.3 h^{-1} \text{Mpc}$ which is comparable to the CLAMATO survey.

Figure 1 shows various physical quantities in the entire light-cone at $z = 2 - 3$, covering $100 h^{-1} \text{cMpc}$ (vertical) $\times 1 h^{-1} \text{cGpc}$ (horizontal path-length) $\times 10 h^{-1} \text{cMpc}$ (depth). From top to bottom panels: total gas overdensity, HI overdensity, temperature, metallicity, and the galaxy distribution color-coded by galaxy stellar masses. One can see visually that the higher mass galaxies are more clustered in higher density regions as expected from their higher clustering strength. Since our simulation box is limited to $100 h^{-1} \text{cMpc}$, we do not have very massive galaxies with stellar masses $M_\star > 10^{12} M_\odot$ at $z \sim 2$. Ideally we would like to simulate larger volumes in the future, however, the box size of $100 - 200 h^{-1} \text{cMpc}$ is currently the sweet spot due to the balance of numerical resolution, large-scale modes of power spectrum, and the computing power of current supercomputers.

Figure 2 shows an example of LoS data as a function of redshift at $z = 2.4 - 2.6$, giving more detailed view of absorption line profiles and density fluctuations. The four panels show, from top to bottom, the normalized transmitted flux (i.e., $\exp(-\tau)$), total gas overdensity, HI overdensity, baryon peculiar velocities, and temperature profiles. One can see that some absorption troughs are slightly shifted from the density peaks due to pe-

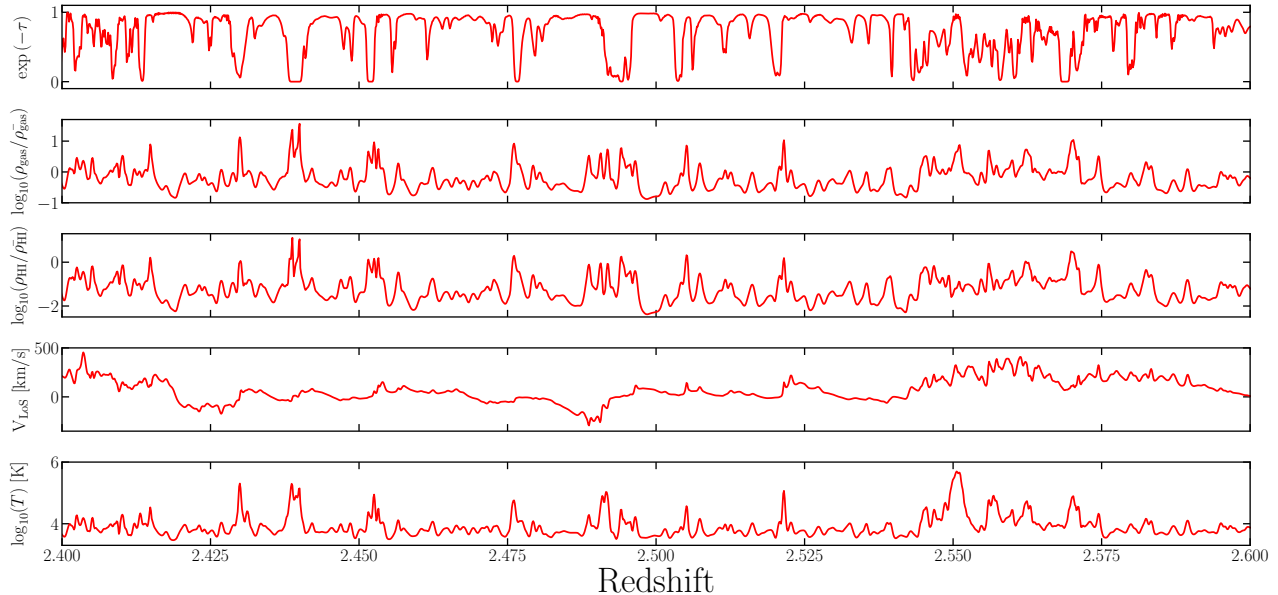


Figure 2. An example of line-of-sight data for $z = 2.4 - 2.6$. From top to bottom: transmitted flux (i.e. $\exp(-\tau)$), total gas overdensity, HI overdensity, peculiar velocity along the LoS, and temperature distribution. One can see that the absorption trough is slightly shifted from the overdensity peaks due to peculiar velocities, and the HI overdensities sometimes do not match with the total gas overdensities in hot overdense regions (e.g. see the features associated with a high- T peak at $z \sim 2.55$.)

cular velocities. When the peculiar velocity is positive (negative), the absorption is redshifted (blueshifted).

In the flat Planck cosmology adopted in this paper, the redshift path of $\Delta z \sim 0.1$ corresponds to a comoving distance of $\Delta r \approx c\Delta z/H(z) \approx c\Delta z/(3.58H_0) \approx 120$ cMpc at $z = 2.4$, which roughly corresponds to one simulation box size. Therefore Fig. 2 is created by using about two simulation boxes of $100 h^{-1}$ cMpc size.

3. RESULTS

3.1. Ly α forest flux PDF

As a starting point of our analysis, we show in Fig. 3 the probability distribution function (PDF) of Ly α forest transmitted flux $F = \langle e^{-\tau} \rangle$. Here the higher value of F means more transmission, i.e., less absorption with lower τ . Panel (a) shows the redshift evolution of flux PDF at $z = 2 - 3$. As the effective optical depth $\tau_{\text{eff}}(z) = -\ln\langle F(z) \rangle$ increases from $z = 2$ to 3 (Becker et al. 2013), the absorption lines with high τ increases, and the plateau at low- F gradually rises. Here, we follow the standard practice of normalizing the simulated transmitted flux to $\tau_{\text{eff}}(z)$ of Becker et al. (2013) in order to account for the uncertain UVB (e.g., Viel et al. 2013b). The peak at high F (> 0.9) instead becomes steeper towards higher values of F .

We also compare the results of different runs in Fig. 3b, and find that the overall shape of the PDF does not change so much except for the slight variations at $F < 0.5$. This is because the majority of absorp-

tion lines are dominated by low-column density systems with high F values. It has been suggested that the Ly α forest statistics is not largely affected by galactic wind because the hot supernova bubbles preferentially expand into the voids without affecting the filaments very much (Theuns et al. 2002; Tepper-García et al. 2013). Cen et al. (2005) suggested that the volume filling factor of metal-enriched bubbles is a strong test for the strength of galactic wind feedback. Both Viel et al. (2013b) and Chabanier et al. (2020) argued that AGN feedback can affect the flux PDF and 1-D power spectrum significantly, but this seems to contradict with the results of Sorini et al. (2020).

In Fig. 3c, we compare our result at $z \sim 2.5$ to the observational data points (Kim et al. 2007; Rollinde et al. 2013). The pink shaded region shows the $1-\sigma$ of all LoS that we have drawn, and the red solid line shows the median of all simulated PDFs from all LoS. We find that most of the observed data points are within $1-\sigma$ scatter of simulated results except for the highest F value bin, and that our simulation is in reasonable agreement with the observational data. The discrepancy at the highest F values is nearly universal among hydrodynamical simulations of the Ly α forest, and in fact likely due to systematic continuum-fitting errors in the observational data (Lee 2012) rather than because of the simulations. Bolton et al. (2017) found that the observational data points were within $2-\sigma$ of the flux PDF from the SHERWOOD simulation, although in about half

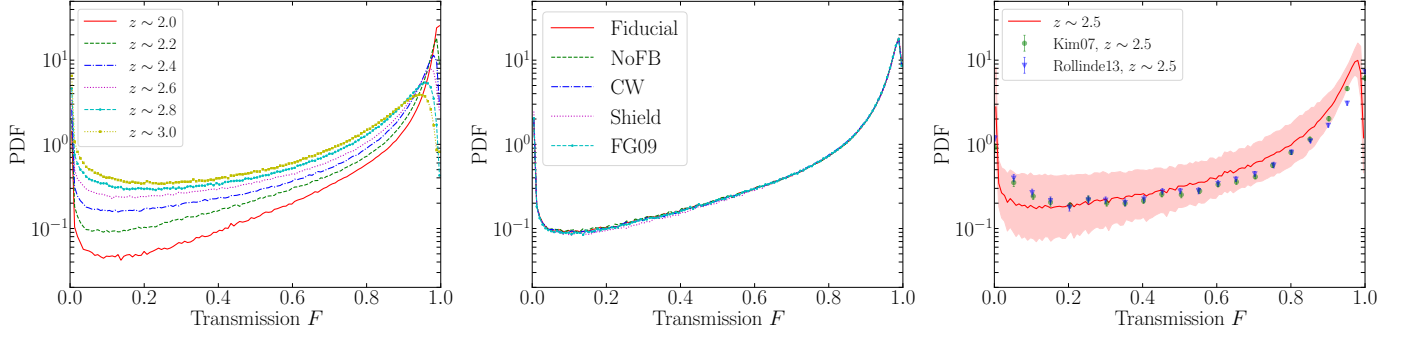


Figure 3. PDFs of Ly α forest transmission flux $F = \langle e^{-\tau} \rangle$ of all LOS from our fiducial run (Osaka18-Fiducial). *Panel (a)* shows the evolution of PDF from $z = 2 - 3$ for the Osaka18-Fiducial run. *Panel (b)* compares the PDF of three different runs at $z = 2$. Only slight variations in the PDFs at low F range are seen. *Panel (c)* compares our result at $z \sim 2.5$ against the observational data by Kim et al. (2007) and Rollinde et al. (2013). The red solid line shows the median value in logarithmic space of PDF, and the pink shaded region shows $1-\sigma$ range.

of the bins, the observational data were below the simulation result by more than $1-\sigma$. They suggested that their simulation might be lacking hot underdense gas because adopting an isothermal temperature–density relation improves the agreement at $0.1 < F < 0.8$. It seems that our simulation does not have this problem as we have a good agreement in the range of $0.1 < F < 0.8$, but we do need to investigate further the exact cause of deviations from observational data at $F < 0.1$.

3.2. 1D Ly α power spectrum

In addition to the flux PDF, the one-dimensional (1D) power spectrum of Ly α forest $P_{1D}(k)$ is another important observed statistic (Croft et al. 1998; McDonald et al. 2006; Palanque-Delabrouille et al. 2013; Chabanier et al. 2019). In their pioneering work, Croft et al. (1998) presented a simple method to recover the shape and amplitude of the power spectrum of matter fluctuations from observations of Ly α forest using a fast Fourier transform (FT) method. Palanque-Delabrouille et al. (2013) measured the $P_{1D}(k)$ using 13821 high-quality quasar spectra from SDSS-III/BOSS DR9 at $z = 2.2 - 4.4$ on scales of $k = 0.001 - 0.02 \text{ km s}^{-1}$. They improved the constraints on cosmological parameters from SDSS by a factor of a few over the previous estimate by McDonald et al. (2006), deriving $\sigma_8 = 0.83 \pm 0.03$ and $n_s = 0.97 \pm 0.02$ assuming a flat- Λ universe with no massive neutrinos, although without considering the astrophysical impacts of feedback in their hydrodynamic simulations. Viel et al. (2013b) examined the $P_{1D}(k)$ using the OWLS cosmological hydrodynamic simulations (Schaye et al. 2010), and argued that the effect of galactic wind is comparable to the uncertainties of observed power spectra, and must be taken into account for a robust and accurate measurement.

Here we follow Croft’s FT method for our calculation of $P_{1D}(k)$ for its simplicity and clarity. Figure 4 presents

$P_{1D}(k)$ from our simulations compared with the observational data of Palanque-Delabrouille et al. (2013); Walther et al. (2018). Some previous numerical works have added a Gaussian noise of $6 - 7 \text{ km s}^{-1}$ to the absorption profile data in order to mimic the observational error due to limited spectral resolution. Instead, here we vary the velocity bin size when we compute the averaged absorption profile to evaluate the impact of spectral resolution. In Fig. 4a, we show $P_{1D}(k)$ for five different velocity bin-size of $\delta_v = 10, 20, 40, 80, \& 160 \text{ km s}^{-1}$. As expected, with smaller spectral bin sizes, the $P_{1D}(k)$ reaches higher k and probe smaller scales. Note that $\delta_v = 160 \text{ km s}^{-1}$ corresponds to $\sim 2 h^{-1} \text{ cMpc}$ in the adopted cosmology. Our result with $\delta_v = 10 \text{ km s}^{-1}$ captures the upper end of $P_{1D}(k)$ very well at high- k , but some differences can be seen at the intermediate scale of $\log k \sim -1.5$ and at the largest scales of $\log k \lesssim -2.5$. But these differences are well within the $1-\sigma$ scatter of all LoSs as shown in Fig. 4b (red shaded region). Given our large $1-\sigma$ scatter, we argue that current observational data points underestimate the uncertainties due to cosmic variance. We repeated our calculation with $128^2 = 16384$ sight-lines, but the $1-\sigma$ scatter range did not change very much, which means that our $P_{1D}(k)$ result is already stable and have converged with robust error with $32^2 = 1024$ sight-lines.

Figure 4c shows the redshift evolution of $P_{1D}(k)$ for the Fiducial run at $z \sim 2.2 - 3.0$. As the effective Ly α optical depth increases towards higher redshift, the normalization of $P_{1D}(k)$ also rises, and our simulation captures this evolution qualitatively well, with similar levels of differences with observational data as in Fig. 4a,b. These differences with the observational data is understandable because we have not fine-tuned our IGM thermal state by tweaking the parameters of temperature–density relation ($T \propto \rho^\gamma$) as other simulation works have

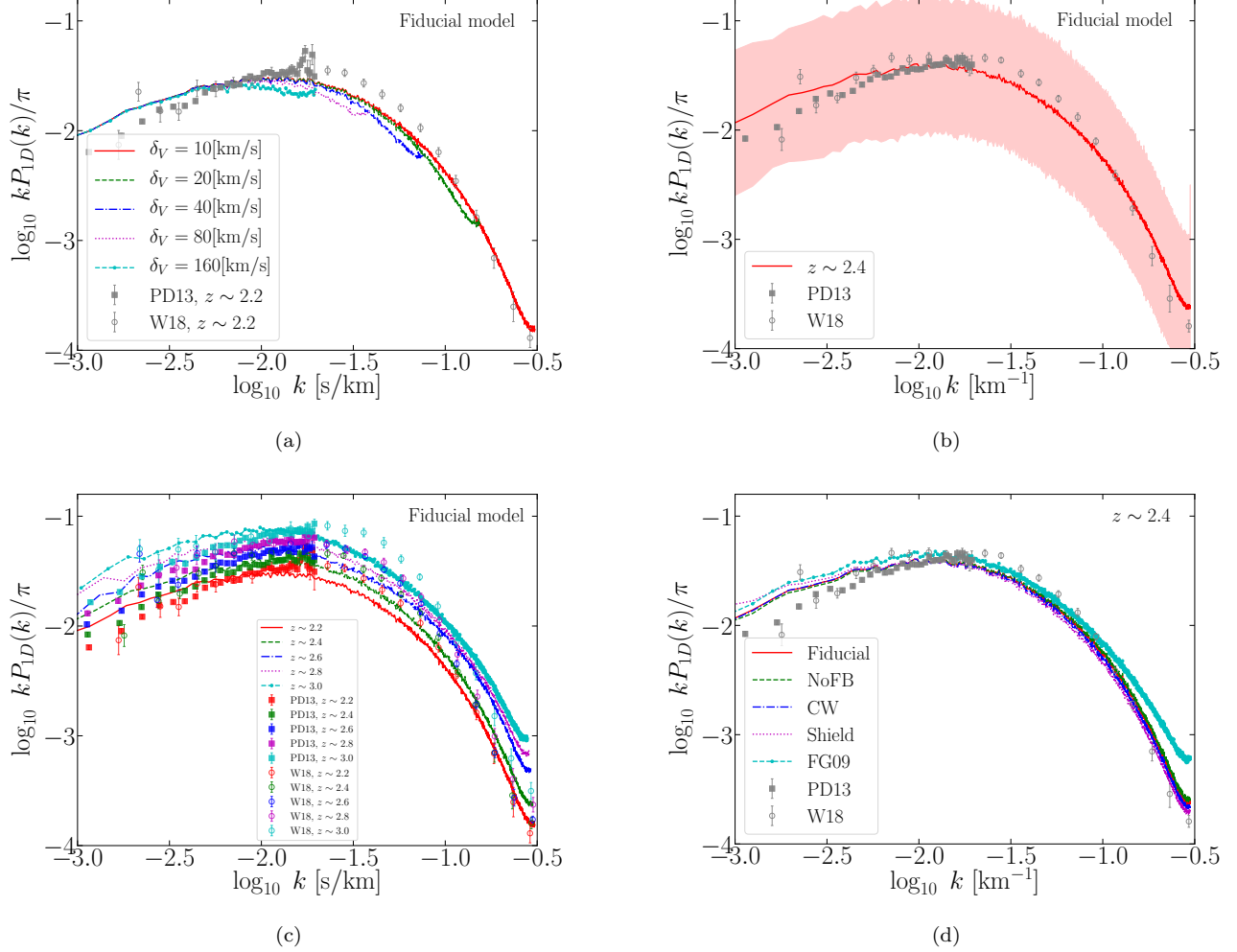


Figure 4. 1D power spectrum of Ly α forest as a function of velocity wave number. *Panel (a)* compares the $P_{1D}(k)$ computed with different δ_v -size for our Fiducial run. As the value of δ_v becomes smaller, one can probe smaller scales more, and the upper end of $P_{1D}(k)$ shifts to higher k with decreasing δ_v . *Panel (b)* shows the 1- σ variance of all LoS in the Fiducial run with the red shaded region, and the median in each bin is shown by the red curve. *Panel (c)* shows the redshift evolution of $P_{1D}(k)$ from $z = 2$ to 3 for the Fiducial model. *Panel (d)* compares $P_{1D}(k)$ from different simulation models given in Table 1. In all panels, the observational data points are from Palanque-Delabrouille et al. (2013, P13) and Walther et al. (2018, W18).

done assuming the Fluctuating Gunn-Peterson Approximation (FGPA; e.g. Croft et al. 1998; Sorini et al. 2018).

3.3. Flux contrast vs. Impact Parameter

We define the Ly α “flux contrast” η_F as follows:

$$\eta_F = -\delta_F = 1 - \frac{F}{\langle F \rangle}, \quad (3)$$

where δ_F is the absorption decrement integrated over a given velocity window within the 1D skewers, and $F = \exp(-\tau)$ is the transmitted flux. The value of η_F increases to unity with stronger absorption due to greater amount of H I. In the opposite limit of smaller τ , η_F approaches zero.

In Figure 5, we present η_F computed for various galaxy samples as a function of impact parameter

b [h^{-1} cMpc] from the galaxies. The general trend is that η_F increases with decreasing b , meaning that the amount of H I increases towards the center of galaxies. This trend is consistent with the earlier simulation results (e.g. Turner et al. 2017; Meiksin et al. 2017; Sorini et al. 2018).

In Figure 5a, we compare η_F computed with different search ranges of $\delta_v = 100, 500, 1000$, & 2000 km s^{-1} , and using the sample of galaxies with stellar masses $M_* \geq 10^9 M_\odot$. To be more precise, for example, for $\delta_v = 100 \text{ km s}^{-1}$, we take the radial path-length of $\delta_v = \pm 50 \text{ km s}^{-1}$ from the closest point to the galaxy of concern. The value of η_F is expected to be higher (i.e. stronger absorption) for smaller δ_v , as it probes only close to galaxies. We see good agreement with the

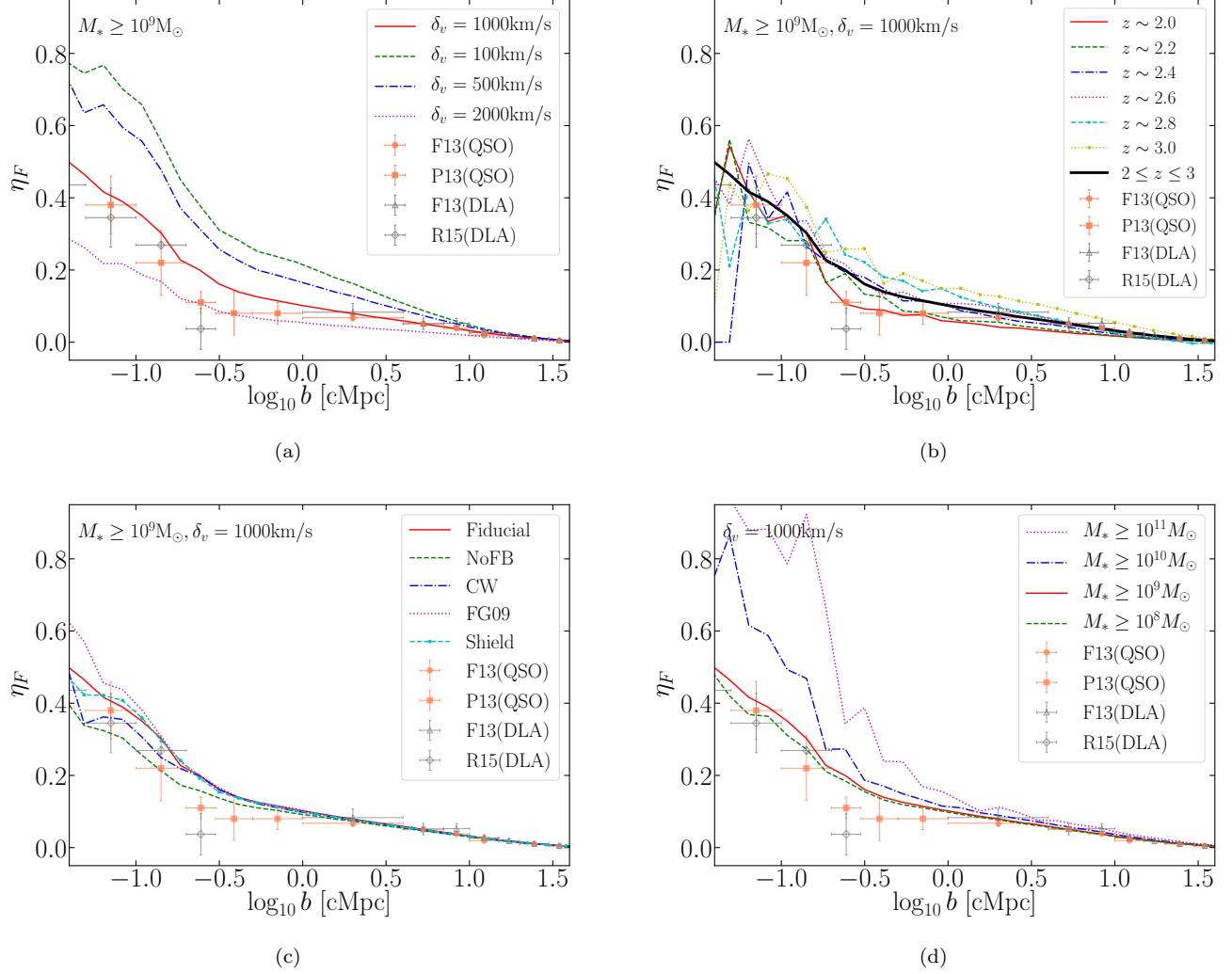


Figure 5. Flux contrast η_F vs. impact parameter b in units of comoving Mpc. *Panel (a)* compares the results computed with different search range δ_v . *Panel (b)*: Redshift evolution of η at $z = 2 - 3$. *Panel (c)*: Model dependency of η_F . The data points with error bars are from Prochaska et al. (2013, orange square) and Font-Ribera et al. (2013, orange circle and grey triangle), and Rubin et al. (2015, grey diamond).

observational data for $\delta_v \geq 1000 \text{ km s}^{-1}$, however, as we see in other panels, the final signal is also dependent on the stellar mass of galaxy sample and the redshift range, so the comparison is not so straight-forward.

Figure 5b shows the redshift evolution of η_F as a function of impact parameter b . We see that the variation of η_F due to model difference is smaller than those due to δ_v or M_* dependence. Some lines become somewhat noisy on small scales due to lack of galaxies to produce robust signals.

Figure 5c shows the results of η_F for different models and simulation runs given in Table 1. This panel was computed with galaxy samples of $M_* \geq 10^9 M_\odot$ and $\delta_v \geq 1000 \text{ km s}^{-1}$. At this time, all the models are mostly within the error bars of current observational data, and the agreement with the data on larger scales of

$b > 1 \text{ cMpc}$ is quite impressive, supporting good agreement between the simulations of ΛCDM model and observations of IGM HI on large scales.

To interpret the model-dependences shown in Fig. 5c, we have to consider the impact of star formation. For example, one might naively expect that there will be more HI gas around galaxies for the No-FB run. However, it is known that galaxies become too dense and compact without galactic wind feedback, and the dense gas in the galaxy is vigorously converted into stars, which leads to the overprediction of galaxy stellar masses. As a result of this overconsumption of gas into stars, the No-FB run in fact has the lowest η_F among all models. In the CW run, the gas is ejected out of galactic potential more efficiently than other models with some overheating of gas (Choi & Nagamine 2011), the amount of HI gas around

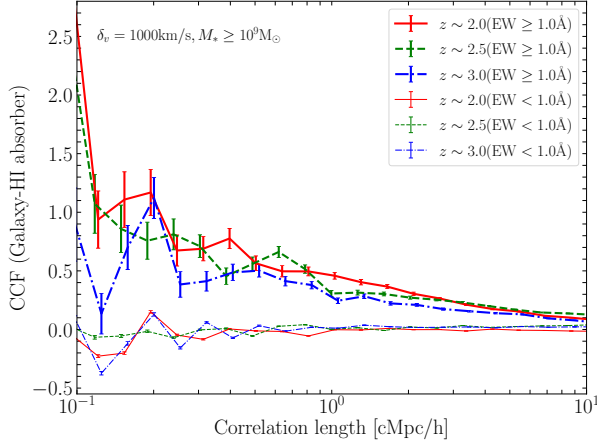


Figure 6. CCF between galaxies ($M_* \geq 10^9 M_\odot$) and HI absorbers with high EW (EW $> 1 \text{ \AA}$; thick lines) and low EW (EW < 1 ; thin lines) as a function of transverse distance between galaxies and LoS. High-EW systems have stronger correlations with galaxies, while low-EW systems are more broadly distributed, hence almost no correlation or negative correlation. See the main text for more details.

galaxies is less in the CW run compared to the Fiducial run. The comparison between the FG09 run and the Shield run also shows that more gas is consumed for star formation in the Shield run due to larger amount of colder gas in the galaxies. These results indicate that it is crucial to treat star formation and feedback in simulations to obtain accurate results on η_F at $b < 300 \text{ ckpc}$.

Figure 5d shows η_F for different galaxy samples with stellar mass ranges of $M_* \geq 10^8, 10^9, 10^{10}$, & $10^{11} M_\odot$. We find higher η_F values for more massive galaxies, as expected from the higher bias of massive galaxies in more massive halos. A good agreement with observational data is seen for the sample of $M_* \geq 10^8$ & $10^9 M_\odot$. This means that the currently observed η_F includes important contributions from the lower mass galaxies of $M_* \leq 10^{10} M_\odot$ rather than just from limited number of massive galaxies.

3.4. Cross-correlation between galaxies and HI

Figure 6 shows the cross-correlation function (CCF) between the simulated galaxies with $M_* \geq 10^9 M_\odot$ and discrete HI absorbers with high EW (EW $> 1 \text{ \AA}$; thick lines) and low EW (EW < 1 ; thin lines) as a function of transverse distance between galaxies and LoS. As for the CCF, we use a simple estimator of $(DD/DR) - 1$, where DD and DR are the number of pairs found in data-data and data-random data sets. Here the EW is simply measured against the transmitted flux of $F = 0, 1$, therefore $\text{EW} = (\text{absorption cross section}) \times 1$. For a more accurate treatment, it requires a photo-ionization calculation using a code like Cloudy, and measure the HI

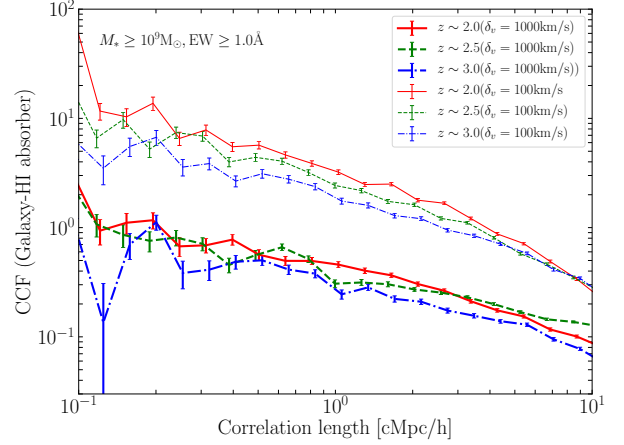


Figure 7. Dependence of CCF on the search range along LoS. The thick lines are for search path-length of $\delta_v = 1000 \text{ km s}^{-1}$, and thin lines are for $\delta_v = 100 \text{ km s}^{-1}$. The latter case is only looking at correlations between close pairs of absorbers and galaxies, hence producing stronger CCF signal. For all cases, galaxies with $M_* > 10^9 M_\odot$ and HI absorbers with high-EW (EW $> 1 \text{ \AA}$) were used.

column density via Voigt profile fitting. We will present such analyses together with metal absorption lines in the future. Here, for a simple examination of dependence of CCF on the HI column density, we divide the sample into two samples of high- and low-EW systems, and compute the CCFs separately at each redshift. In other words, our analysis presented here is performed with unsmoothed, finely sampled HI absorption lines compared to the actual observations.

The high-EW systems have stronger correlations with galaxies as expected, while the low-EW systems are more broadly distributed in space, hence almost no correlation (or even slightly negative correlation on small scales) relative to the galaxies. Note that the ordinate is in a linear scale in this plot to show the negative correlation at the same time. A weak redshift evolution is visible in Fig. 6, with stronger correlations at $z = 2$ than at $z = 3$ due to the evolution in τ_{eff} (Becker et al. 2013). The Poisson error bars are computed as $(1 + \text{CCF})/\sqrt{D_{\text{gal}} D_{\text{abs}}}$, where D_{gal} and D_{abs} are the number of galaxy pairs and absorber pairs in each bin, respectively.

When computing the pairs for the CCF, it is not so obvious how deeply one should search for those pairs along the LoS. In order to examine the impact of search range δ_v , we repeat the CCF calculation with two different values of $\delta_v = 1000$ & 50 km s^{-1} , and show the results in Fig. 7. We first sit on a galaxy, and search for the HI absorbers within $\pm \delta_v$ from the systemic velocity of the galaxy along the LoS. The thick and thin lines are with $\delta_v = 1000 \text{ km s}^{-1}$ and 100 km s^{-1} , respec-

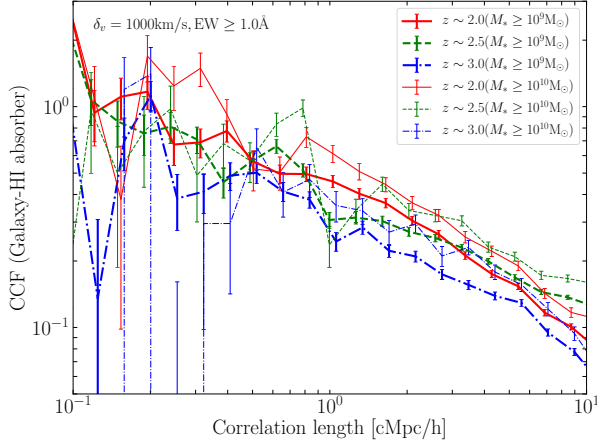


Figure 8. Dependence of CCF on the stellar mass of galaxies of concern. The thick lines are for galaxies with $M_\star > 10^9 M_\odot$, and thin lines are for those with $M_\star > 10^{10} M_\odot$. For all cases, HI absorbers with high-EW ($\text{EW} > 1 \text{ \AA}$) and the search range of $\delta_v = 1000 \text{ km s}^{-1}$ were used.

tively. The latter case is only looking at the correlations between close pairs of absorbers and galaxies, hence producing stronger CCF signals. For all cases, galaxies with $M_\star > 10^9 M_\odot$ and high-EW absorber sample were used.

In Figure 8, we show the dependence of CCF signal on galaxy stellar mass. The number of galaxies with $M_\star > 10^{10} M_\odot$ becomes smaller at $z = 3$ in our simulation, and the number of CCF pairs also becomes less, resulting in the somewhat noisy CCF signal on small scales. (For example, there are 3515 galaxies between $2.9 < z < 3.1$, which corresponds to two simulation snapshots of $100 \text{ cMpc}/h$ box.) At least, we see that the overall CCF signal is stronger for the $M_\star > 10^{10} M_\odot$ sample (thin lines) than for the $M_\star > 10^9 M_\odot$ sample (thick lines). This is consistent with the stellar-mass trend which we saw in Fig. 5d.

Figure 9 shows the 2D CCF between galaxies and HI with contours showing 16 levels between min/max in logarithmic scale. Consistently with the observational and simulation results of Turner et al. (2017), we find the finger-of-god signature of elongation along the LoS direction with a stronger CCF signal. It is encouraging that we detect the finger-of-god signal, but it requires further analysis of gas dynamics to figure out what’s really causing this signature, e.g., inflow/outflow. To detect this effect, Fig. 9 shows that it requires a transverse resolution of $< 1 \text{ cMpc}/h$.

3.5. Comparison with the ‘Mukae plot’

Even if one does not have spectroscopic data, photometric data of galaxies are also useful to investigate macroscopic relations between gas and galaxies. The combination of spectroscopic and imaging surveys are powerful if

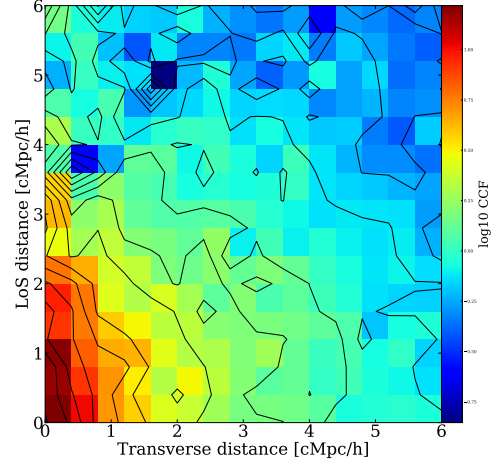


Figure 9. Two-dimensional CCF between galaxies and HI with contours showing 16 levels between the min/max values ($-0.85/1.22$) in logarithmic scales.

we could perform IGM tomography. For example, Fig. 8 of Mukae et al. (2020) compares the LAE overdensity filaments with gas filaments from the IGM tomography.

Mukae et al. (2017) detected a weak correlation between galaxy overdensity (δ_{gal}) and Ly α absorption decrement (δ_F) in cylinders with a base radius of $r = 5'$ ($\sim 2.5 \text{ pMpc}$ at $z \sim 2.5$) and a cylinder length of 25 pMpc which corresponds to their photometric redshift uncertainty. Their galaxies lie at $2 < z < 3$. In the following, we call this correlation plot between δ_{gal} and δ_F a ‘Mukae plot’. They found a weak negative correlation of

$$\delta_F = a \delta_{\text{gal}} + b \quad (4)$$

with $a = -0.14^{+0.06}_{-0.16}$ and $b = -0.17^{+0.06}_{-0.06}$.

In Fig. 10a, we show the results from our simulation estimated with similar parameters as Mukae et al. (2017). The red dots represent measurement with each cylinder in our simulation, which show a greater scatter than Mukae’s result (grey data points with error bars and their best-fit). The red solid line is the least-square fit to simulation result with $1-\sigma$ error bars with $a = -0.084 \pm 0.0021$ and $b = -0.099 \pm 0.00081$. Our simulation result has a shallower slope than Mukae’s fit, however, still consistent within the error. The number of data points by Mukae et al. (2017) is much smaller than our simulated data points, and their fit may have been affected strongly by the outliers with low $\delta_{\langle F \rangle}$ values (~ -0.4).

In Fig. 10b, we compare our results against Liang et al. (2020, submitted), who made similar measurements of δ_{gal} (to be precise, 2642 Ly α emitters at $z \sim 2.2$) using

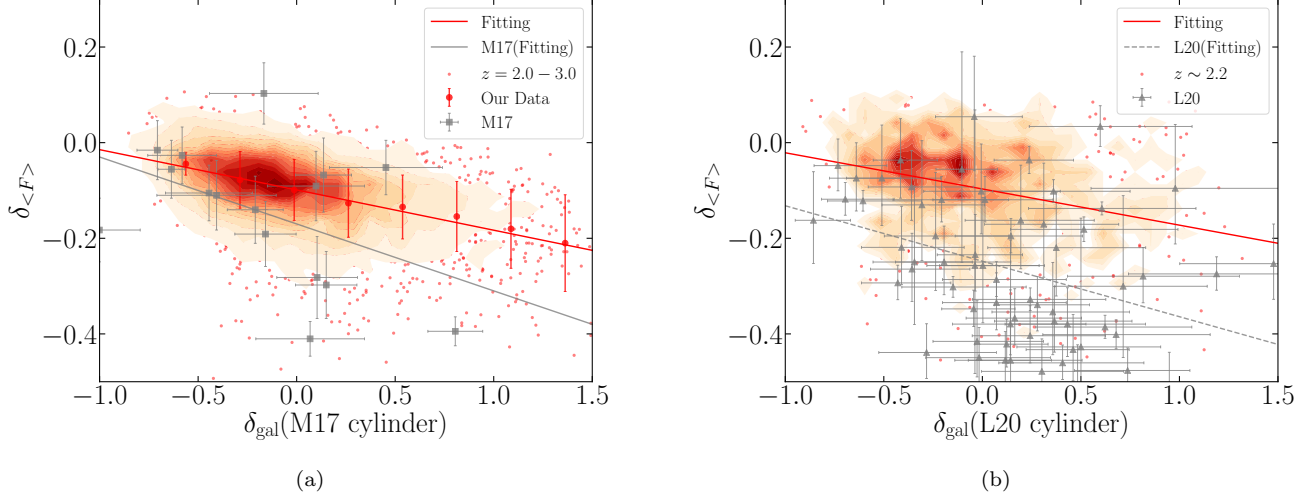


Figure 10. Relation between flux contrast δ_F vs. galaxy overdensity δ_{gal} , compared against the observational data *Panel (a)* compares the simulation result against the observational data of Mukae et al. (2017, grey data points and their linear regression fit shown by the gray line). Each red data point corresponds to one LOS in our simulation, with median in each δ_{gal} -bin and linear regression result shown by the red solid line. *Panel (b)*: Same as panel (a), but now comparing against the observational data by Liang et al. (2020, submitted). Here, δ_F is computed within the scale of $15 h^{-1} \text{cMpc}$, i.e., 21.4cMpc assuming $h = 0.7$, and δ_{gal} is computed using a cylinder with an aperture radius $(10 \text{cMpc}) \times 62.5 \text{cMpc}$ (length along the LoS $\approx \text{FWHM}$ of NB387 filter). Note that the path-length to compute δ_F and the cylinder size for δ_{gal} are different between panels (a) & (b).

a cylinder with a base aperture radius of 10cMpc and a length of 62.5cMpc (the FWHM of the NB387 filter) along LoS. As for δ_F , the radial path-length of averaging is done over $10 h^{-1} \text{cMpc}$, i.e., 21.4cMpc assuming $h = 0.7$, and the center of an absorber is searched as the absorption peak around $3,862 \pm 35 \text{\AA}$ ($z \approx 2.15 - 2.20$). They found positive correlation between LAE overdensity and the effective Ly α optical depth estimated from 63 eBOSS quasar spectra. Liang et al. gave the best-fit results of $a = -0.116^{+0.018}_{-0.022}$ and $b = -0.248^{+0.082}_{-0.093}$ (for all four fields) and $a = -0.227^{+0.026}_{-0.023}$ and $b = -0.258^{+0.096}_{-0.114}$ (without the J0210 field).

Correspondingly, we made similar measurements from our simulation using the same cylinder size and path-length, with the only difference of placing our cylinders at the redshift of concern, covering $\pm L/2$ where $L = 21.4 \text{cMpc}$. Our best-fit result gives $a = -0.0664 \pm 0.00476$ and $b = -0.0938 \pm 0.00238$, which is close to Liang’s result. The number of data points of Liang et al. is much larger with more scatter than those of Mukae’s, which could be one of the reasons for the shallower slope. See their § 5.1 for further discussions on the sample bias. It is nevertheless interesting that similar galaxy–HI correlation is obtained even in an extreme system such as the MAMMOTH region (Cai et al. 2016; Liang et al. 2020, submitted) to that of Mukae’s more general field. The exact value of normalization parameter b is probably not so important at this point, as each observational result is based on a different sample of galaxies with dif-

ferent normalization. But Liang’s data might otherwise show that LAEs might prefer HI-rich environment than general galaxies, and the spatial offset of LAEs from general galaxies were also observed in the results of Momose et al. (2020b).

Liang et al. (2020, submitted) also presented the results from our simulation using different galaxy samples of $M_{\star} = 10^8 - 10^9$, $10^8 - 10^9$, and $10^9 - 10^{10} M_{\odot}$, and showed that the slope ‘ a ’ became slightly shallower for more massive galaxy sample, but not by much. This trend is consistent with naive expectation that the more massive galaxies are associated with deeper potential wells and more abundant HI gas around them. It is also consistent with our earlier result shown in Fig. 5d, where a stronger flux contrast is detected around more massive galaxies. However, we also note that this naive expectation can be easily broken if the photoionization due to radiation from galaxies or quasars is strong, producing the proximity zone around massive systems. In fact, the Mukae’s galaxy sample had $M_{\star} \geq 10^{9.7} M_{\odot}$, which is on the massive side of the simulated galaxy sample, but yet showed a steeper result than the simulation. Therefore the differences in the slope is difficult to explain simply by the stellar mass of the galaxy sample.

Given that the dependence of the slope on galaxy stellar mass is weak in our simulation, Liang et al. proposed that the attenuation of Ly α emission by the intergalactic HI might be the more dominant effect in lowering δ_{LAE} (and hence making the slope ‘ a ’ steeper) rather

than the galaxy stellar mass of the sample. Mukae et al. (2020) also pointed out the photoionization effect by the radiation from galaxies and quasars, producing proximity zones. To verify these arguments, we would have to perform Ly α radiation transfer calculations through IGM, which we plan to carry out in the future.

3.6. Flux contrast around a proto-cluster

Proto-clusters have been one of the interesting focus of high- z galaxy studies. Given that it is a biased region with early evolution of density field, studying proto-clusters can give us important insight in the early structure formation and help us to check the Λ CDM model during the critical phase when the structure formation is strongly driven by the gravitational instability and the formation of dark matter halos. Using proto-clusters as a cosmological probe can signify the importance of environmental effect of cosmic star formation rate density (e.g., Chiang et al. 2017), and the filamentary distribution of cosmic gas (e.g., Umeata et al. 2019).

The definition of proto-clusters may vary depending on the authors, but usually it is either a high concentration of galaxies at high redshift (e.g., Toshikawa et al. 2016, 2017), or specifically meaning progenitors of present-day galaxy clusters in numerical simulations. In the actual observations, one cannot follow the time evolution of a system at a certain redshift to the present day, so one has to rely on other theoretical arguments, e.g., estimate the dark matter halo mass and refer to the results of N -body simulation for statistical connection between high- z sample and low- z sample.

Future IGM tomography studies will be able to identify numerous proto-clusters without relying on spectroscopic follow-up of galaxies. In fact, Lee et al. (2016) discovered an extended IGM overdensity with deep absorption troughs at $z = 2.45$ associated with a pre-discovered proto-cluster at the same redshift. They estimated that this IGM overdensity is associated with dark matter mass of $M_{\text{DM}}(z = 2.45) \sim 1.1 \times 10^{14} h^{-1} M_{\odot}$, which will later grow into a galaxy cluster with $M_{\text{DM}}(z = 0) \sim 3 \times 10^{14} h^{-1} M_{\odot}$. Krolewski et al. (2018) also reported a discovery of a cosmic void at $z \sim 2.3$ using 3D Ly α tomographic map. Therefore it would be desirable to study tomographic properties of proto-clusters in cosmological hydrodynamic simulations with full physics, and see if we find similar physical properties.

Figure 11 shows the projected quantities around the proto-cluster at $z \sim 2.1$ with halo mass of $M_{\text{h}} = 9.4 \times 10^{13} h^{-1} M_{\odot}$ and virial radius of $R_{\text{v}} = 1.1 \text{ cMpc}$. This is the most massive system in our light-cone data set. There is a clear high-overdensity region in the center of upper left panel of dark matter density field. Cor-

respondingly the high-temperature ($T \gtrsim 10^7 \text{ K}$) intra-cluster gas is also visible in the center of the lower left panel, which would emit X-rays. The central region of this proto-cluster is already enriched to $\log(Z/Z_{\odot}) \sim -1.5$ by $z = 2.1$. On the other hand, it is interesting to see that the proto-cluster is not so visible in the HI overdensity map in the upper right panel, because the HI gas is more localized in the centers of galaxies and not as prominent as the hot X-ray emitting intra-cluster gas within the proto-cluster.

Figure 12 shows the flux contrast as a function of impact parameter from the center of the proto-cluster. On large scales of $b > 1 \text{ cMpc}$, the flux contrast signal converges to the large-scale IGM signal, but we see an enhancement of signal at $b < 200 \text{ ckpc}$ towards the center of the proto-cluster, even though it's not really visible to our eyes in the upper right panel of Fig. 11. In particular, in the inner-most bin of $b \simeq 100 \text{ ckpc}$, we see an enhancement by a factor of ~ 2 over the observed data points. The proto-cluster flux contrast is in-between those for the galaxy population of $M_{\star} \geq 10^{10}$ and $M_{\star} \geq 10^{11} M_{\odot}$. This is reasonable, as we are approaching to the proto-cluster center where the brightest cD galaxy may be developing in the core. Our result is also in line with that of Miller et al. (2019), in the sense that the high- τ sightlines are dominated by galaxies and DLAs, whereas most of the sightlines simply have lower τ . When the contribution from proto-cluster galaxies are averaged over in spherical shells, it can produce the increasing flux contrast towards the proto-cluster center.

In Fig. 12, we are also showing the data points from Mukae et al. (2020), who studied the 3D distribution of HI around quasars in the MAMMOTH-1 nebula (Cai et al. 2017) at $z = 2.3$ using HI tomography technique. They discovered that the HI absorption is weak around the quasar, suggesting a proximity zone of photoionized gas. We also note that Momose et al. (2020b) detected weaker HI absorption within central few cMpc around AGNs, and that the maximum absorption is at $r = 5 - 6 h^{-1} \text{ cMpc}$, again suggesting proximity effect. (The differences between the data points by Prochaska et al. (2013) and Mukae et al. (2020) can be reconciled with anisotropic emission from quasars. See § 6.3 of Prochaska et al. (2013) for further discussions.) Therefore, if we want to study 3D distribution of HI around quasars and AGNs, a realistic model of AGN feedback is desired in simulations. On the other hand, Sorini et al. (2020) showed that, on average, the impact of AGN is not so strong compared to stellar feedback on Ly α forest statistics. It is clear that more detailed studies are needed to figure out when and how AGN feedback af-

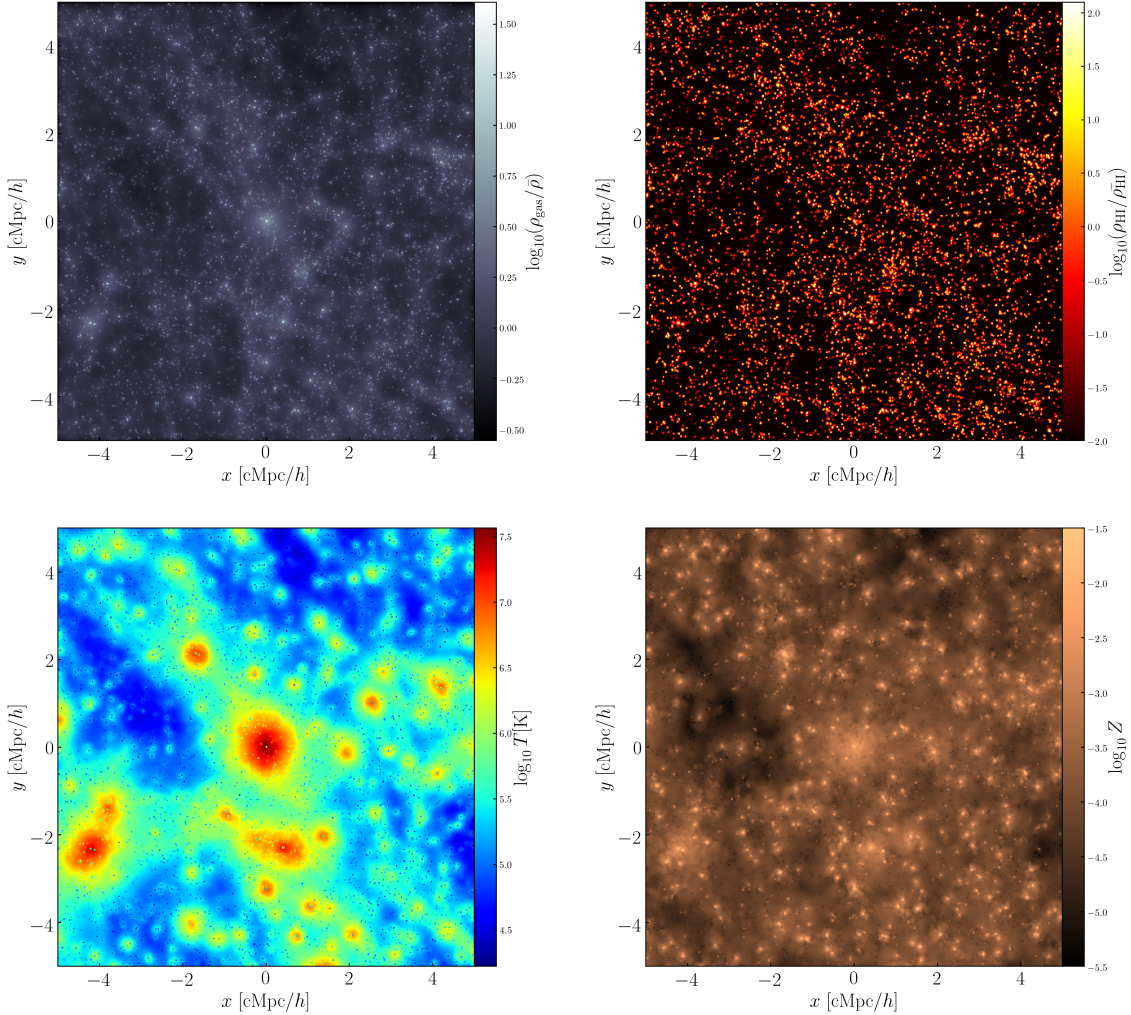


Figure 11. Projected maps of various quantities (gas overdensity, HI overdensity, temperature, metallicity, from top-left to bottom-right, respectively) in the proto-cluster region, which is the most massive system in our light-cone data. The mass of the proto-cluster is $M_h = 9.4 \times 10^{13} h^{-1} M_\odot$ at $z \sim 2.1$, and the virial radius is $R_v = 1.1$ cMpc.

fects $\text{Ly}\alpha$ forest statistics, and we plan to do so in the future.

4. DISCUSSION & SUMMARY

In preparation for the upcoming Subaru PFS survey and other major telescopes such as TMT and JWST, we produce the light-cone and LoS data sets at $z = 2 - 3$ using the GADGET3-OSAKA cosmological hydrodynamic simulations with star formation and SN feedback models. We compute various $\text{Ly}\alpha$ forest statistics including 1D flux PDF, 1D power spectrum, and flux con-

straint as a function of transverse distance from galaxy centers and a proto-cluster.

We draw 1024 LoS to compute $\text{Ly}\alpha$ forest data, and find that 1D flux PDF shows overall good agreement with observations, although with a large $1\text{-}\sigma$ scatter around the mean. We have checked that the scatter and the mean does not change very much even if we draw 16384 LoS, which means that our results do not change very much by increasing the number of LoS any more. Given our results, it is possible that the current observational data points are underestimating the scatter due

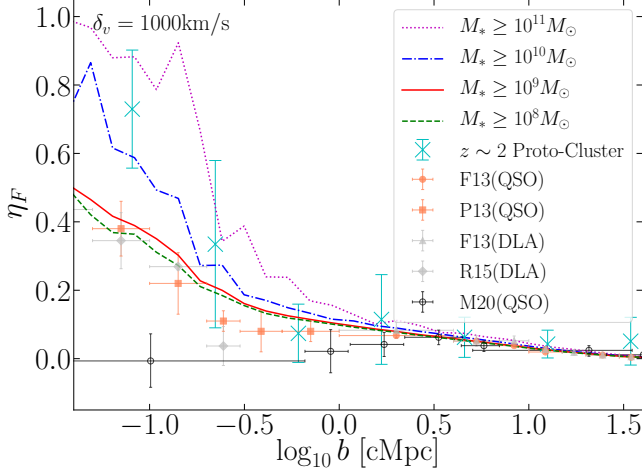


Figure 12. Flux contrast around the proto-cluster shown in Fig. 11 at $z \sim 2$ as a function of impact parameter from the protocluster center. The blue crosses show the average flux contrast in each radial bin, and each data point is an average of 8 LoS with the error bar showing the min/max scatter. The other observational data points and lines are the same as in Fig. 5d and shown for comparison. Additionally, black open circles are from Mukae et al. (2020), possibly indicating quasar proximity effect.

to cosmic variance within $\sim 100 h^{-1} \text{cMpc}$ scale. The redshift evolution of the flux PDF is as expected, where the fraction of low-transmission lines increases with increasing τ_{eff} towards higher redshift. The variation of flux PDF is not so significant due to changes in the SN feedback model and self-shielding treatment.

The simulated 1D Ly α power spectra show more intricate deviations from observations, and requires further analyses to understand them. Our Fiducial model captures the higher k modes well at $\log k > -1.3$ at $z \sim 2.4$, but at the same time underpredict the power at intermediate scale of $\log k \sim -1.5$, and then overpredict at the large scale of $\log k < -2.5$. This may have to do with the fact that we have not tuned our thermodynamic parameters (e.g. gas temperature) like the FGPA method using N -body simulations to match the observations. Different models (NoFB, CW, Shield, FG09) deviate from the Fiducial run, but not as much to describe all the deviations that we described above. In the future, we will continue to examine the 1D Ly α power spectra using higher resolution and larger box-size simulations.

Perhaps the most direct and easy to understand statistics is the flux contrast η_F as a function of impact parameter b from galaxies (Fig. 5). On large-scales of $b > 1 h^{-1} \text{cMpc}$, we find good agreement with observational estimates and the previous result by Lukić et al. (2015), which supports the correctness of the ΛCDM model and the large-scale structure that it pre-

dicts. On the other hand, on small scales, we find significant variations due to different parameters, such as the galaxy mass, probing depth, redshift, and feedback models. Overall our results show good agreement with currently available observations, however, we find an important dependence of η_F on galaxy stellar masses, where more massive galaxies are surrounded by more abundant HI gas with higher flux contrast. If one combines all the signals from all galaxies and average them over, then the stronger signal from more massive galaxies ($M_* \geq 10^{11} M_\odot$) is diluted by that of lower mass galaxies, and the flux contrast appears to be reduced in the proximity of galaxies.

We also see some (but not so significant; $\sim 20 - 30\%$) variations in η_F on small scales depending on the physical treatment of feedback, self-shielding of gas, star formation, and UVB. It is somewhat counter-intuitive that the No-FB run has the lowest contrast, which is probably because much of the cold gas is consumed by star formation in the high-density galactic center. The CW run is the second lowest, owing to its efficient removal of gas from galactic potential with strong galactic wind. The Fiducial and the Shield model have about the same level of η_F on small scales. The FG09 run has the highest level of η_F relative to the HM12 model in the Fiducial run. While these deviations are interesting to discuss, the variation due to galaxy stellar mass and the probed path length (δ_v) is larger than that due to different feedback models. The redshift evolution of η_F is not so strong during $z = 2 - 3$, but clearly the contrast at $z = 3$ is higher than that at $z = 2$ at all scales of $100 \text{ ckpc} < b < 20 \text{ cMpc}$ due to higher τ_{eff} . We find strong flux contrast around a proto-cluster at $z \sim 2$ in our simulation, which is comparable to that for the galaxies with $M_* \geq 10^{10} - 10^{11} M_\odot$ (Fig. 12). This result certainly lends support for finding more proto-clusters via HI tomography and massive galaxies associated with it.

The cross-correlation between galaxies and HI absorbers shows expected trends. For example, the higher EW sample is more correlated with galaxies than the lower EW sample, because more neutral HI gas is expected to be closer to the galaxies. More massive galaxies have stronger CCF signal on larger scales of $> 500 \text{ ckpc}$, but the signal becomes noisy at smaller scales. The redshift evolution of CCF signal is not so strong, but we do see that it is stronger at $z = 2$ than at $z = 3$ at least on larger scales of $> 1 \text{ cMpc}$, as the cosmic structure develops and galaxy clustering becomes stronger. Our 2D CCF result (Fig. 9) shows the finger-of-god feature similarly to Turner et al. (2017), but it would require a transverse resolution of $< 1 \text{ cMpc}$ res-

olution in the IGM tomography to study this effect in more detail observationally. Theoretically we will study the gas dynamics that causes this effect in more detail in our subsequent papers, e.g., the impact of cold accretion flows and galactic outflows on the 2D CCF.

We also examined the correlation between galaxy overdensity δ_{gal} vs. flux contrast δ_F , and compared the results with those of Mukae et al. (2017) and Liang et al. (2020, submitted) using the same cylinder size as their measurements. Our simulation result shows a large scatter from a larger number of cylinders than the observations, and a shallower slope in the best-fit relation than the observations (Fig. 10). These differences could be due to a few different things, such as different galaxy sample used, cosmic variance, or photoionization effect by the radiation emitted by galaxies or quasars. This comparison study using the Mukae plot is not as definitive as the flux contrast at this point, however, it provides a support for such a methodology utilizing photo- z galaxy sample that are more widely available with cheaper observational costs.

The examination of a protocluster in our simulation (Figs. 11, 12) also bring up interesting directions for our future research. In particular, we see a hot X-ray emitting gas in the center of the proto-cluster, but at the same time we don't see diffuse HI distribution near the center. Rather, it seems that the HI absorption is mostly contributed from individual galaxies rather than diffuse intra-protocluster medium, and when averaged over the spherical shells, it produces an enhancement of flux contrast in the central few 100 cpc. This result seems to be in line with that of Miller et al. (2019), in the sense that the high- τ sightlines are dominated by galaxies and

DLAs, whereas most of the sightlines simply have lower τ . In our future work, we plan to follow up on these issues utilizing higher resolution zoom-in simulations of proto-clusters.

In this paper, we focused on the relative distribution of galaxies and HI, and did not touch on the metal absorption lines, which we will discuss in our future publications. The cross-correlation studies between galaxies, HI and metals will certainly give us useful information on the interplay between them and to learn more about star formation and feedback. The astrophysics in this subject is quite rich, and at the same time, quite challenging to get it all right, as we need to have a good understanding of cosmology, galaxy formation, star formation, feedback and chemical enrichment of the IGM, and link them all together to have a full picture.

KN acknowledges useful discussions with J. X. Prochaska. KN is grateful to Volker Springel for providing the original version of GADGET-3, on which the GADGET3-OSAKA code is based on. Our numerical simulations and analyses were carried out on the XC50 systems at the Center for Computational Astrophysics (CfCA) of the National Astronomical Observatory of Japan (NAOJ), OCTOPUS at the Cybermedia Center, Osaka University, and Oakforest-PACS at the University of Tokyo as part of the HPCI system Research Project (hp180063, hp190050, hp200041). This work is supported by the JSPS KAKENHI Grant Number JP17H01111 (KN), 19H05810 (KN), JP18H05868 (KGL), and JP19K14755 (KGL). KN acknowledges the travel support from the Kavli IPMU, World Premier Research Center Initiative (WPI), where part of this work was conducted.

APPENDIX

A. OBSERVATIONAL INFORMATION

In 2020s, we enter the era of massively multiplexed spectroscopy which enables us to study the IGM from small (\sim kpc) to large scales (\sim 100 cMpc). This means that a unique era is coming soon where we can test the simulated universe by observations with a greater precision (i.e., the era of ‘*precision structure formation*’). In this appendix, to set the stage, we review some of the details of Subaru PFS and other near-future facilities. In particular, there is at the time of writing no published description of the planned PFS IGM tomography program, and so we will provide some details here.

A.1. Subaru PFS (2023)

The Prime Focus Spectrograph (PFS; Sugai et al. 2015) is expected to be installed on the prime focus of Subaru Telescope in 2020–2021. Its wide field-of-view (1.25 deg^2) and large collecting area (8.2 m in diameter) are unique among other facilities. There is continuous wavelength coverage is $3800 \text{ \AA} - 1.26 \mu\text{m}$ with three cameras, at medium resolving power ($R \equiv \lambda/\Delta\lambda \sim 2000 - 4000$). Currently, a large collaboration is planning to execute a survey with \sim 300 nights from 2023 through 2027, called the SSP (Subaru Strategic Program). This SSP is envisaged as having

three components: the Cosmology Survey, Galactic Archeology Survey, and the Galaxy Evolution Survey — an early version of this SSP plan is outlined in Takada et al. (2014), although the details therein are no longer up-to-date.

The PFS Galaxy Evolution Survey, in particular, will be a deep survey covering approximately 14 deg^2 across three of the Subaru Hyper SuPrime Camera Deep imaging fields (Aihara et al. 2018). Across multiple visits, over 340,000 spectra will be obtained across multiple target classes ranging from $0.7 \lesssim z \lesssim 7$. One of the major goals of this project is to generate a 3-D tomographic map of the optically-thin HI at $2.1 < z < 2.6$ with average transverse sight-line separation of $\sim 4 \text{ cMpc}$ using 16,000 star-forming galaxies ($g < 24.7$; see more details in Table A.1) at $2.5 < z < 3.5$ acting as background probes of intervening absorbing neutral gas (i.e. IGM tomography). While this sightline density is similar to that of the CLAMATO Survey (Lee et al. 2018), the PFS program will be approximately $50\times$ larger in area and volume, covering a combined comoving volume of $4 \times 10^7 \text{ cMpc}^3$. One of the primary products envisaged from these observations is the Wiener-filtered absorption maps of the large-scale structure traced by the diffuse Ly α forest, which will provide sufficient detail to recover the cosmic web on scales of $\sim 4 h^{-1} \text{ Mpc}$ (Lee & White 2016; Krolewski et al. 2017). More recently, Horowitz et al. (2019) presented the TARDIS analysis framework which allows direct inference of the underlying density field, which allows reconstruction of smaller scale structures ($\sim 2 h^{-1} \text{ Mpc}$) than Wiener filtering.

Table 2. Subaru PFS IGM Tomography Targets

Target Class	Redshift	Selection	Exposure	Targeted Objects	Number/PFS FOV
	Range		Time (hrs)	(Useful Spectra)	(1.25 deg^2)
IGM Background (bright)	2.5-3.5	$y < 24.3, g < 24.2$	6	8300 (5810)	770
IGM Background (faint)	2.5-3.5	$y < 24.3, 24.2 < g < 24.7$	12	14000 (9800)	1790
IGM Foreground	2.1-2.6	$y < 24.3$	6	22000 (15400)	8308

In addition to the LBGs and QSOs targeted as Ly α forest background sources, there will also be a category of ‘IGM Foreground’ galaxies selected to be at $2.1 < z < 2.6$, i.e. coeval with the Ly α absorption. This class of targets will be broadly selected among galaxies with $y < 24.3$ (see Table A.1) to span a wide range

of galaxy properties. Subaru PFS spectra should have sufficient spectral resolution and signal-to-noise to measure the IGM metal absorption lines (e.g., Mg II, Si IV and C IV) simultaneously, as well as O II emission in the near-infrared. With approximately 15,000 useful spectra expected from this target class, we expect to be able to robustly test the trends discussed in this paper.

REFERENCES

- Aihara, H., Arimoto, N., Armstrong, R., et al. 2018, Publications of the Astronomical Society of Japan, 70, <https://academic.oup.com/pasj/article-pdf/70/SP1/S4/23692189/psx066.pdf>, s4.
- Altay, G., Theuns, T., Schaye, J., Crighton, N. H. M., & Dalla Vecchia, C. 2011, ApJL, 737, L37
- Aoyama, S., Hou, K.-C., Shimizu, I., et al. 2017, MNRAS, 466, 105
- Becker, G. D., Hewett, P. C., Worseck, G., & Prochaska, J. X. 2013, MNRAS, 430, 2067
- Bird, S., Vogelsberger, M., Sijacki, D., et al. 2013, MNRAS, 429, 3341
- Bolton, J. S., & Becker, G. D. 2009, MNRAS, 398, L26
- Bolton, J. S., Puchwein, E., Sijacki, D., et al. 2017, MNRAS, 464, 897
- Cai, Z., Fan, X., Peirani, S., et al. 2016, ApJ, 833, 135
- Cai, Z., Fan, X., Bian, F., et al. 2017, ApJ, 839, 131
- Cen, R., Miralda-Escudé, J., Ostriker, J. P., & Rauch, M. 1994, ApJL, 437, L9
- Cen, R., Nagamine, K., & Ostriker, J. P. 2005, ApJ, 635, 86
- Chabanier, S., Bournaud, F., Dubois, Y., et al. 2020, arXiv e-prints, arXiv:2002.02822
- Chabanier, S., Palanque-Delabrouille, N., Yèche, C., et al. 2019, JCAP, 2019, 017
- Chevalier, R. A. 1974, ApJ, 188, 501
- Chiang, Y.-K., Overzier, R. A., Gebhardt, K., & Henriques, B. 2017, ApJL, 844, L23

- Choi, J.-H., & Nagamine, K. 2011, *MNRAS*, 410, 2579
- Cirasuolo, M., Afonso, J., Carollo, M., et al. 2014, in Society of Photo-Optical Instrumentation Engineers (SPIE) Conference Series, Vol. 9147, Proc. SPIE, 91470N
- Cowie, L. L., Songaila, A., Kim, T.-S., & Hu, E. M. 1995, *AJ*, 109, 1522
- Croft, R. A. C., Weinberg, D. H., Katz, N., & Hernquist, L. 1998, *ApJ*, 495, 44
- Dalton, G., Trager, S. C., Abrams, D. C., et al. 2012, in Society of Photo-Optical Instrumentation Engineers (SPIE) Conference Series, Vol. 8446, Proc. SPIE, 84460P
- Dawson, K. S., Schlegel, D. J., Ahn, C. P., et al. 2013, *AJ*, 145, 10
- Faucher-Giguère, C., Lidz, A., Zaldarriaga, M., & Hernquist, L. 2009, *ApJ*, 703, 1416
- Font-Ribera, A., Arnau, E., Miralda-Escudé, J., et al. 2013, *JCAP*, 5, 018
- Haardt, F., & Madau, P. 2012, *ApJ*, 746, 125
- Hernquist, L., Katz, N., Weinberg, D. H., & Miralda-Escudé, J. 1996, *ApJL*, 457, L51
- Horowitz, B., Lee, K.-G., White, M., Krolewski, A., & Ata, M. 2019, *ApJ*, 887, 61
- Iršič, V., Viel, M., Berg, T. A. M., et al. 2017, *MNRAS*, 466, 4332
- Kim, J.-H., Abel, T., Agertz, O., et al. 2014, *ApJS*, 210, 14
- Kim, J.-h., Agertz, O., Teyssier, R., et al. 2016, *ApJ*, 833, 202
- Kim, T. S., Bolton, J. S., Viel, M., Haehnelt, M. G., & Carswell, R. F. 2007, *MNRAS*, 382, 1657
- Krolewski, A., Lee, K.-G., Lukić, Z., & White, M. 2017, *The Astrophysical Journal*, 837, 31.
- Krolewski, A., Lee, K.-G., White, M., et al. 2018, *ApJ*, 861, 60
- Lee, K.-G. 2012, *ApJ*, 753, 136
- Lee, K.-G., & White, M. 2016, *ApJ*, 831, 181
- Lee, K.-G., Hennawi, J. F., Stark, C., et al. 2014, *ApJL*, 795, L12
- Lee, K.-G., Hennawi, J. F., White, M., et al. 2016, *The Astrophysical Journal*, 817, 160.
- Lee, K.-G., Krolewski, A., White, M., et al. 2018, *ApJS*, 237, 31
- Lukić, Z., Stark, C. W., Nugent, P., et al. 2015, *MNRAS*, 446, 3697
- McDonald, P., Seljak, U., Cen, R., et al. 2005, *ApJ*, 635, 761
- McDonald, P., Seljak, U., Burles, S., et al. 2006, *ApJS*, 163, 80
- McKee, C. F., & Ostriker, J. P. 1977, *ApJ*, 218, 148
- Meiksin, A., Bolton, J. S., & Puchwein, E. 2017, *MNRAS*, 468, 1893
- Meiksin, A., & White, M. 2004, *MNRAS*, 350, 1107
- Miller, J. S. A., Bolton, J. S., & Hatch, N. 2019, *MNRAS*, 489, 5381
- Miralda-Escudé, J., Cen, R., Ostriker, J. P., & Rauch, M. 1996, *ApJ*, 471, 582
- Momose, R., Shimizu, I., Nagamine, K., et al. 2020a, arXiv e-prints, arXiv:2002.07334
- Momose, R., Shimasaku, K., Kashikawa, N., et al. 2020b, arXiv e-prints, arXiv:2002.07335
- Mukae, S., Ouchi, M., Kakiichi, K., et al. 2017, *ApJ*, 835, 281
- Mukae, S., Ouchi, M., Cai, Z., et al. 2020, *ApJ*, 896, 45
- Nagamine, K., Choi, J., & Yajima, H. 2010, *ApJL*, 725, L219
- Overzier, R. A. 2016, *A&A Rv*, 24, 14
- Palanque-Delabrouille, N., Yèche, C., Borde, A., et al. 2013, *A&A*, 559, A85
- Palanque-Delabrouille, N., Yèche, C., Lesgourgues, J., et al. 2015, *JCAP*, 2015, 045
- Planck Collaboration, Ade, P. A. R., Aghanim, N., et al. 2016, *A&A*, 594, A13
- Prochaska, J. X., Hennawi, J. F., Lee, K.-G., et al. 2013, *ApJ*, 776, 136
- Rahmati, A., Pawlik, A. H., Raičević, M., & Schaye, J. 2013, *MNRAS*, 430, 2427
- Ravoux, C., Armengaud, E., Walther, M., et al. 2020, arXiv e-prints, arXiv:2004.01448
- Rollinde, E., Theuns, T., Schaye, J., Pâris, I., & Petitjean, P. 2013, *MNRAS*, 428, 540
- Rubin, K. H. R., Hennawi, J. F., Prochaska, J. X., et al. 2015, *ApJ*, 808, 38
- Saitoh, T. R. 2017, *AJ*, 153, 85
- Schaye, J., Dalla Vecchia, C., Booth, C. M., et al. 2010, *MNRAS*, 402, 1536
- Shimizu, I., Inoue, A. K., Okamoto, T., & Yoshida, N. 2016, *MNRAS*, 461, 3563
- Shimizu, I., Todoroki, K., Yajima, H., & Nagamine, K. 2019, *MNRAS*, 484, 2632
- Smith, B. D., Bryan, G. L., Glover, S. C. O., et al. 2017, *MNRAS*, 466, 2217
- Sorini, D., Davé, R., & Anglés-Alcázar, D. 2020, arXiv e-prints, arXiv:2005.08971
- Sorini, D., Oñorbe, J., Hennawi, J. F., & Lukić, Z. 2018, *ApJ*, 859, 125
- Springel, V. 2005, *MNRAS*, 364, 1105
- Springel, V., & Hernquist, L. 2003, *MNRAS*, 339, 289
- Stinson, G., Seth, A., Katz, N., et al. 2006, *MNRAS*, 373, 1074

- Sugai, H., Tamura, N., Karoji, H., et al. 2015, *Journal of Astronomical Telescopes, Instruments, and Systems*, 1, 035001
- Takada, M., Ellis, R. S., Chiba, M., et al. 2014, *PASJ*, 66, R1
- Tasitsiomi, A. 2006, *ApJ*, 648, 762
- Tepper-García, T., Richter, P., & Schaye, J. 2013, *MNRAS*, 436, 2063
- Theuns, T., Viel, M., Kay, S., et al. 2002, *ApJL*, 578, L5
- Toshikawa, J., Kashikawa, N., Overzier, R., et al. 2016, *The Astrophysical Journal*, 826, 114.
- Toshikawa, J., Uchiyama, H., Kashikawa, N., et al. 2017, *Publications of the Astronomical Society of Japan*, 70, 1708.09421
- Turner, M. L., Schaye, J., Crain, R. A., et al. 2017, *MNRAS*, 471, 690
- Tytler, D., Paschos, P., Kirkman, D., Norman, M. L., & Jena, T. 2009, *MNRAS*, 393, 723
- Umehata, H., Fumagalli, M., Smail, I., et al. 2019, *Science*, 366, 97
- Viel, M., Becker, G. D., Bolton, J. S., & Haehnelt, M. G. 2013a, *PhRvD*, 88, 043502
- Viel, M., Lesgourgues, J., Haehnelt, M. G., Matarrese, S., & Riotto, A. 2005, *PhRvD*, 71, 063534
- . 2006, *Physical Review Letters*, 97, 071301
- Viel, M., Schaye, J., & Booth, C. M. 2013b, *MNRAS*, 429, 1734
- Walther, M., Hennawi, J. F., Hiss, H., et al. 2018, *ApJ*, 852, 22
- Weinberg, D. H., Burles, S., Croft, R. A. C., et al. 1998, *ArXiv Astrophysics e-prints*, astro-ph/9810142